International Journal of Heat and Mass Transfer 219 (2024) 124885

Contents lists available at ScienceDirect

International Journal of Heat and Mass Transfer

journal homepage: www.elsevier.com/locate/ijhmt

A coupled model of finite element method and Mie theory for heat transfer inside expanded perlite vacuum insulation panels (VIPs) at high temperatures

Mohammad Reza Jalali, Dron Kaushik, Sankarshan Verma, Harjit Singh *

Institute of Energy Futures, College of Engineering, Design and Physical Sciences, Brunel University London, Uxbridge, UB8 3PH, UK

ARTICLE INFO

Keywords:
Mie theory
Finite element method
Vacuum insulation panels
Expanded perlite
High temperatures

ABSTRACT

The present study introduces the first coupled model of the finite element method and Mie theory that predicts the heat transfer mechanism inside the expanded perlite vacuum insulation panels at a temperature range of 300–800 K. The finite element method is applied to discretise the governing equation of the steady state heat transfer and the three-dimensional Fourier's law is used. COMSOL Multiphysics is the finite element numerical solver which predicts solid and gaseous thermal conductivity inside the VIPs. Moreover, Mie theory predicts the radiative conductivity. Heat transfer radiation is superimposed on the heat transfer through conduction. The model is capable of predicting total thermal conductivity of VIPs at high temperatures $\geq$ 500 K, which makes it a unique model with clear advantage over previously developed numerical models. The numerical predictions of the developed coupled model are validated experimentally. The predictions of the coupled model are in good agreement with the experimental measurements, which indicate the capability of the developed model to predict the mechanisms of heat transfer at high temperatures. For instance, the values of total thermal conductivity for numerical prediction and experimental measurement, at 557 K, are 14.6 and 14.7$\pm$1.2 mW/m/K, respectively, excellently agreeing within $\pm$ 8.9 %.

1. Introduction

Globally the usage of thermal energy in buildings is one of the main causes of carbon dioxide (CO_2) emission with a significant impact on environment and economics. Consequently, efforts are on to enhance the efficiency of energy use. Governments all around the world have encouraged the constructional companies to build more buildings with high thermal resistance insulations preventing heat energy loss. Last year's sudden rise of energy prices after Ukraine-Russia war has highlighted the importance of reducing energy consumed in all sectors of the world economy [1].

Vacuum Insulation Panels (VIPs) owing to a high thermal resistance are excellent replacement for conventional building insulation. A typical VIP used in buildings is a rigid panel containing an evacuated inner core board inside an outer barrier envelope [2].

VIPs core materials are open porous foams, powders and fibres. Fumed silica (SiO_2) powder is the most popular material to produce VIPs core, because its small-scale pore size with the order of 10 nm causes low solid and gaseous thermal conductivities [3]. However, fumed silica is an expensive material (at ≈4$/kg); therefore, research to identify cheaper alternative materials to replace fumed silica is very contextual. Expanded perlite, glassy amorphous mineral rock, is reported appropriate candidate to be used in VIPs core [4]. A larger particle size and pore size of expanded perlite cause a larger amount of heat transferred through VIPs [2,5,6]. To eliminate the effect of a larger pore size on gaseous thermal conductivity a higher level of vacuum is required in the case of expanded perlite core VIPs. This problem can be resolved by introducing fumed silica in the expanded perlite [2]. Aggregates of fumed silica powder are reported to migrate into larger pores of expanded perlite reducing the resultant pore size. Heat transfer mechanisms in a VIP include solid conduction, gaseous conduction, radiation and coupling effects [4,7,8]. The conductive mechanisms are controllable. For instance, vacuumisation significantly reduces gaseous conductivity, use of low-density materials reduce solid conductivity, and use of opacifiers decrease radiative conductivity [2]. The study of heat transfer mechanisms in VIPs enables the researchers to design better quality VIPs with a lower production cost. In recent years, researchers have studied the application of fumed silica, fibres and foams in VIPs [3,

* Corresponding author.
E-mail address: harjit.singh@brunel.ac.uk (H. Singh).

https://doi.org/10.1016/j.ijheatmasstransfer.2023.124885
Received 21 July 2023; Received in revised form 1 October 2023; Accepted 26 October 2023
Available online 2 November 2023

9,10]. They have developed numerical models and performed experimental measurements to better understand the heat transfer mechanism [11–13]. However, there are a very few studies reporting efforts to understand the mechanism of heat transfer in VIPs made of expanded perlite. For example, Verma and Singh [5] developed the first numerical model to calculate the thermal conductivity of expanded perlite particle arranged in two different packing structures, simple cubic packing and the hexagonal close packing. Finite element method was applied to discretise the steady state heat transfer equation and three-dimensional Fourier's law used. Investigating the effect of particle size, intra-particle pore size, porosity, internal gas pressure and contact ratio on the thermal conductivity, they experimentally validated the developed numerical model. According to diffusion equation, the radiative thermal conductivity is proportional to the cube of the mean absolute temperature (T^3), therefore, radiation is the dominant factor amongst heat transfer mechanisms at high temperatures (600–800 K) [7,8].

Whilst literature reviews such as Bouquerel et al. [14] have been recently published, to learn more about the studies relevant to VIP research, authors have decided to provide a complete review on the subject of numerical predictions, theoretical investigations and experimental measurements of the mechanics of heat transfer in VIPs as follows.

1.1. Numerical model developed to study solid, gaseous and radiative conductivities in VIPs

Zhang et al. [15] developed a one-dimensional finite volume numerical model to combine radiation and conduction to predict the total thermal conductivity of fibrous insulation at various temperatures and core pressures. The predictions of the model were verified by developing an apparatus to measure heat transfer through high-alumina fibrous insulation. Kan et al. [11] developed a numerical model to investigate the effect of micro structure of porous core materials and vacuum level on total thermal conductivity. Jang et al. [12] introduced a model which combined radiative and conductive heat transferred through studying depth-wise conduction phenomena in stacked radiation shields. Foray et al. [13] developed a numerical model based on finite element method coupled with accompanying X-ray tomography measurements to determine the heat flow in composite aerogels. Yang et al. [16] proposed a numerical model to predict the effects of the fibre volume fraction and fibre diameter on effective thermal conductivity of fused silica fibre/aerogel composites core VIPs at 300–1300 K. Caps et al. [17] applied Mie model and Monte Carlo method to predict radiative flux in high temperature insulation, and they showed that the diffusion approximation is valid for calculation of radiative heat transfer even in the presence of strong anisotropic scattering. Yang et al. [18] proposed to combine Rosseland equation, Mie scattering theory, Beer's law and Subtractive Kramers–Kronig (SKK) relation to calculate radiative thermal conductivity of ultrafine fibrous insulation. Jang et al. [19] applied Monte Carlo method to determine radiative heat transfer in the isotropic scattering and pure backward scattering layers in VIPs; predictions agreed with the diffusion approximation. Choi et al. [20] proposed a statistical formulation to determine the radiative heat transfer in VIPs with results being in a good agreement with those obtained from diffusion approximation, Monte Carlo method and discrete ordinate interpolation method. Xie et al. [21] developed a fractal-intersecting sphere model to consider the effect of gas conduction and solid conduction and Mie theory to calculate Rosseland extinction coefficient and radiative thermal conductivity for silica aerogel composites. Liu et al. [22] proposed an inverse method based on a real-valued genetic algorithm optimization to calculate the effective thermal conductivity of silica aerogel composites at 280–1080 K from experimentally measured temperature data.

1.2. Experimental and theoretical studies of the effect of opacifiers on radiative conductivity

Singh et al. [3], studied heat exchange phenomena in VIPs to better understand radiative thermal conductivity of fumed silica mixed with different IR-opacifiers proportions and a composition with minimum thermal conductivity was determined. Arduini et al. [23] studied the effect of opacifiers on the radiative heat transfer in cellular polymeric foams by calculating specific extinction coefficient of opacified foams from individual spectral extinction coefficients of polymers and opacifiers. Feng et al. [24] experimentally examined the effect of opacifiers on specific extinction coefficient in fumed silica core VIPs. Zhu et al. [25] theoretically determined the extinction performance of different opacifiers, and reported optimal temperature-dependant particle size and doping amounts of opacifiers that maximise the Rosseland mean extinction coefficient and minimise the total thermal conductivity of core composites. Wang et al. [26] investigated the radiative properties of opacified (metallic or metallized) cylindrical fibres and spherical powders employing electromagnetic theory and concluded that fine metal fibres provided an excellent thermal resistance against radiation. Caps and Fricke [27] experimentally investigated radiative heat transfer and solid conductivity of load-bearing VIPs containing perlite, precipitated silica, and fumed silica mixed with different opacifiers. Effect of the physical load on the solid conductivity was studied as well. Feng et al. [28], studied the radiative heat transfer for thermal insulating composites of fumed silica, opacifiers, and fibres at high temperatures. They calculated the spectral radiative properties including scattering and absorption to better understand radiative heat attenuation mechanisms. Liang et al. [9], developed and experimentally validated a theoretical model to calculate total thermal conductivity of VIPs with aerogel composite cores. Effect of aerogel density on the total thermal conductivity was studied. Verma et al. [6] experimentally evaluate the effect of opacifiers on perlite core VIPs reporting that opacifiers significantly reduce total thermal conductivity.

1.3. Studies on radiative heat transfer in VIPs made of open porous foams, powders and fibres

Kuhn et al. [29] introduced a method to determine the infrared-optical properties of loose powder beds via directional-hemispherical transmission and reflection measurements whilst considering particle size, refractive index, and density. Hager et al. [30] reported that the radiant heat transfer rates in laminar arrays of high-emissivity fibres with diameter much larger than the wavelengths of the emitted radiation was proportional to the cube of the mean absolute temperature of the sample. Baillis et al. [31] experimentally determined absorption coefficient, scattering coefficient, and phase function of open cell carbon foams. Tong and Tien [32] predicted the radiant heat flux in lightweight fibrous insulations using two-flux and linear anisotropic scattering solution. The radiative properties of lightweight fibrous insulations were obtained based on the extinction coefficient. Fricke and Caps [33] characterised VIPs made of fibres, powders, or porous gels based on their infrared optical thickness. They observed that whilst the solid and radiative conductivities were superimposed additively in optically thick insulations, a complex coupling mechanism causes the total thermal conductivity to be larger than the sum of the solid and radiative components in optically thin insulations.

1.4. Studies on perlite core VIPs and fumed silica core VIPs at temperature range of 300–1000 K

Beikircher and Demharter [7] studied radiative heat transport in perlite at 300 °C through extinction coefficient measurements using Fourier transform infrared (FTIR) spectroscopy and measured coupling between solid and gas conductivities. Rottmann et al. [4] based on their measurements between 295 K and 1073 K reported that solid

conductivity was very small and the radiative heat transport was significantly high at high temperatures in expanded perlite cores. Diffusion model was applied to calculate the radiative heat transfer. Rottmann et al. [8] investigated the radiative heat transfer in VIPs made of perlite and various opacifiers at 1073 K using FTIR spectrometry. Alam et al. [2] studied the thermo-physical properties of expanded perlite-fumed silica composites experimentally. Nitrogen sorption technique, mercury intrusion porosimetry and transmission electron microscopy were applied to study the effect of pore size on thermal conductivity. Sonnick et al. [34] investigated precipitated silica as a core material VIPs and determined the coupling effect between gaseous and solid thermal conductivities.

In the present study, the numerical model developed by Verma and Singh [5] is coupled with Mie theory to investigate heat transfer mechanisms, specifically in expanded perlite core VIPs experiencing temperatures of 300–800 K. The radiative conductivity is predicted by Mie theory and solid and gaseous conductivities by applying finite element method to solve the steady state heat transfer equations. Sections 2 and 3, respectively, outline the Mie theory implementations and predictions. Section 4 includes the governing equations for solid and gaseous conductivities and their numerical discretisation. Section 5 presents the results for radiative, solid and gaseous thermal conductivities of expanded perlite, Section 6 experimental validation of the developed numerical model and Section 7 summary of the main findings.

The assumptions considered in the present model are:

- Mie theory is used to predict the extinction coefficient of material. Particles are assumed to be spherical with a radius of the order of magnitude of the wavelength [35]. Scattering occurs independently on each particle and no phase relation exists between different particles.
- For solid and gaseous finite element model, it is assumed that particles are spherical and only have one size with a simple cubic packing.
- While combining the models, it is assumed that the solid and gaseous conduction phenomenon happens parallel with radiative heat transfer as the material is considered optically thick [33], i.e., the infrared photons are absorbed, scattered and re-emitted while travelling inside the medium.

2. Implementation of radiative diffusion equation and Mie model

Radiative diffusion Eq. (1) is a simple relation between radiative heat conductivity and total effective mass-specific extinction coefficient:

$$\kappa_r = \frac{16\sigma n^2 T_r^3}{3\rho e_R^*(T_r)} \tag{1}$$

where κ_r is the radiative conductivity, σ is the Stefan–Boltzmann constant, n is the complex refractive index, T_r is the radiation temperature, ρ is the bulk density and $e_R^*(T_r)$ is the total effective mass-specific extinction coefficient.

Total effective mass-specific extinction coefficient which is also known as mass-specific Rosseland mean extinction coefficient is the sum of the absorption and scattering coefficients. In the present study, Mie model is applied to determine the spectral mass-specific extinction coefficient, $e_\lambda^*(\lambda)$, and its value is replaced in Eq. (2) to calculate mass-specific Rosseland mean extinction coefficient:

$$\frac{1}{e_R^*(T_r)} = \int_{\lambda_1}^{\lambda_2} \frac{1}{e_\lambda^*(\lambda)} \frac{\partial \varepsilon_{\lambda b}}{\partial \varepsilon_b} \, d\lambda \tag{2}$$

where λ is the wavelength, $\varepsilon_{\lambda b}$ is the spectral hemispherical blackbody flux, and ε_b is the hemispherical blackbody flux.

The partial derivative of blackbody emissive power $(\partial \varepsilon_{\lambda b} / \partial \varepsilon_b)$ is calculated using Eq. (3):

$$\frac{\partial \varepsilon_{\lambda b}}{\partial \varepsilon_b} = \frac{\pi C_1 C_2 \sigma^{1/4}}{2\lambda^6 \varepsilon_b^{5/4}} \frac{\exp\left[(C_2/\lambda)(\sigma/\varepsilon_b)^{1/4}\right]}{\left\{\exp\left[(C_2/\lambda)(\sigma/\varepsilon_b)^{1/4}\right]-1\right\}^2} \tag{3}$$

$$\text{and } \varepsilon_b = \sigma T_r^4 \tag{4}$$

where C_1 and C_2 are constant and T_r is the radiation temperature. Transmission and reflection spectra for perlite in the wavelength range of 2 μm $\leq \lambda \leq$ 20 μm are measured using FTIR spectroscopy.

Spectral mass-specific extinction coefficient and mass-specific Rosseland mean extinction coefficient obtained from rigorous Mie model and FTIR measurement are compared with each other to verify the Mie model's predictions. Mie model calculates the exact solution to the electromagnetic scattering and absorption for spherical and cylindrical particles. In the present study, the perlite particles are assumed to have a spherical geometry. To calculate spectral mass-specific extinction coefficient using Mie theory, the complex refractive index of the perlite particles is obtained for wavelength range of 2 μm $\leq \lambda \leq$ 20 μm.

The complex refractive index is:

$$n = m + ik \tag{5}$$

where m is the real part and k the imaginary part of complex refractive index.

The calculation of the complex refractive index, Eq. (5), for each wavelength includes (a) applying Hilbert transform to calculate the real part m and (b) using Eq. (6) to obtain the imaginary part k.

$$k(\lambda) = \frac{\lambda \rho_0 \ln\left(\frac{1}{\tau(\lambda)}\right)}{4\pi \rho_{\mathrm{KBr}} \delta} \tag{6}$$

where τ is the infrared transmittance of the perlite sample measured by the use of FTIR spectrometry at infrared wavelengths from 2 to 20 μm, ρ_0 is the density of the loose perlite, ρ_{KBr} is the density of the potassium bromide (KBr), δ is the thickness of the sample pellet containing both perlite and KBr.

According to the literature [36] Hilbert transform can be used to calculate complex refractive index of the sample given that the sample under investigation is optically thin. Hence, while making samples for FTIR analysis, we used optically thin pallets of core materials mixed with KBr. This makes the data acceptable for Hilbert transform. To verify that the prepared samples are optically thin, optical thickness of KBr pellet was calculated through Eq. (7).

$$\alpha = \rho^* e_R^*(T_r)\, \delta \tag{7}$$

where α is the optical thickness of core material sample, δ the pellet thickness, ρ^* the density of core material in KBr pellet and $e_R^*(T_r)$ the mass-specific Roseland mean extinction coefficient.

Criterion for optical thickness is that a material sample with $\alpha \leq$15 is considered as optically thin [39]. $e_R^*(T_r)$ is obtained from Fig. 1b as 140 $\mathrm{m^2 kg^{-1}}$ and the density of the core material in the FTIR pellet and pellet thickness are $\rho^* = 18\ \mathrm{kgm^{-3}}$ and $\delta = 3.1 \times 10^{-4}$ m, respectively. Replacing these values in Eq. (7) optical thickness is calculated as $\alpha =$ 0.78, therefore, the core material sample is optically thin.

The MATLAB's toolbox function computes Hilbert transform. Mie model predicts the relative cross-sections extinction in terms of the infinite series as shown in Eq. (8).

$$Q_{\mathrm{ext}} = Q_{\mathrm{abs}} + Q_{\mathrm{sc}} = \frac{\lambda^2}{2\pi} \sum_{j=0}^{\infty} (2j+1)\, Re\left[a_j(n,x) + b_j(n,x)\right] \tag{8}$$

where Q_{ext} is the relative cross-section extinction, Q_{abs} is the relative cross-section absorption, Q_{sc} is the relative cross-section scattering, a_j

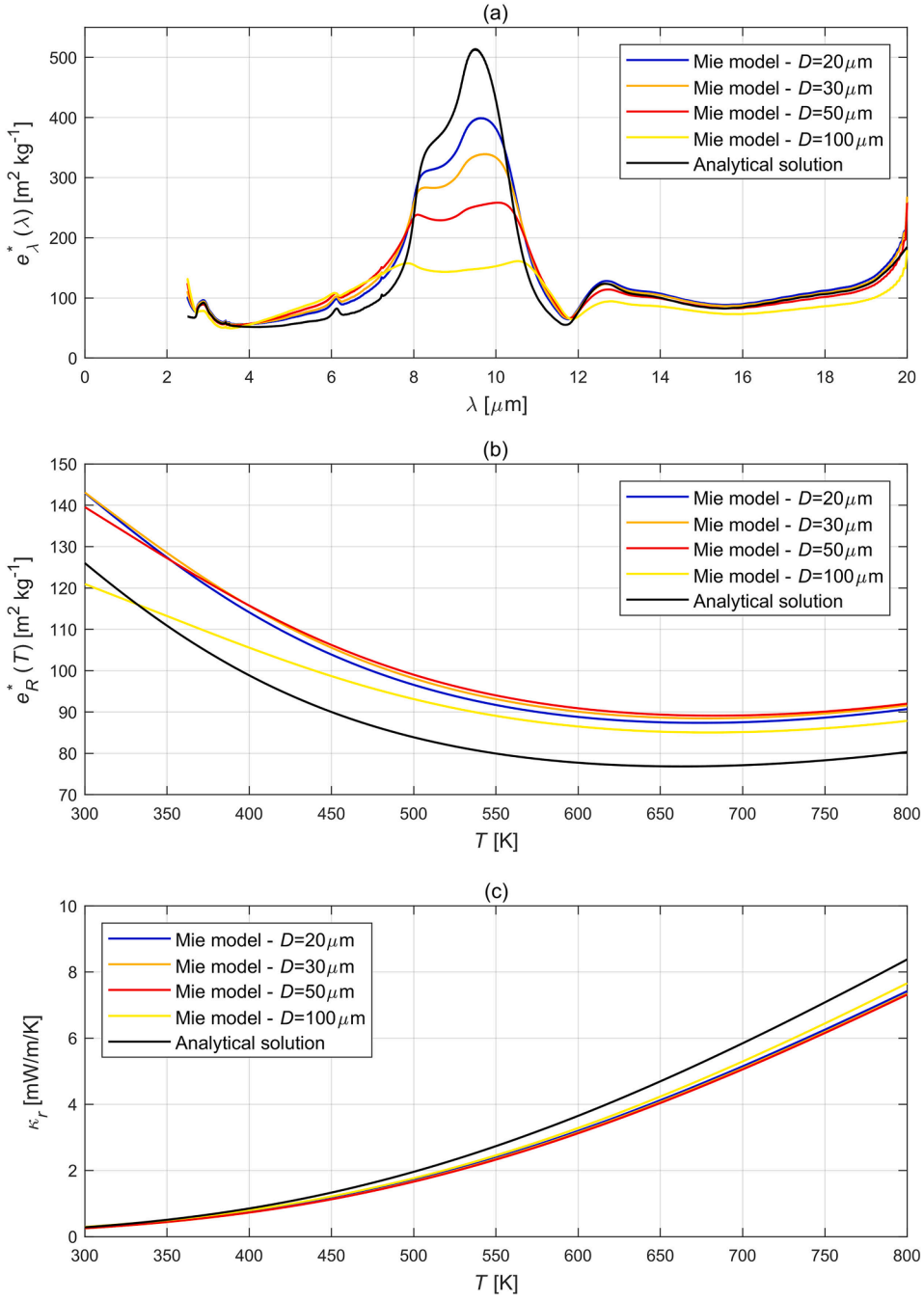

Fig. 1. Comparison between Mie model predictions and the analytical solution for perlite (ρ=230 kgm^{-3}) – (*a*) spectral mass-specific extinction coefficient (*b*) mass-specific Rosseland mean extinction coefficient and (*c*) radiative conductivity. (For interpretation of the references to color in this figure legend, the reader is referred to the web version of this article.)

and b_j are the scattering coefficients which depend on the complex refractive index (n) and the particle size parameter ($x = \pi d/\lambda$). a_j and b_j expressed in terms of the Ricatti-Bessel functions and computed using MATLAB built-in Bessel functions.

Mie model spectral mass-specific extinction coefficient is calculated using Eq. (9):

$$e^*_\lambda(\lambda) = AQ_{\text{ext}}(\lambda, d) \tag{9}$$

where A is the geometrical cross-section and d is the particle diameter [37,38] (Flowchart 1).

To analytically obtain the spectral mass-specific extinction coefficient Beer's law is applied:

$$e^*_\lambda(\lambda) = \frac{\ln\tau}{L\rho^*} \tag{10}$$

where τ is the infrared transmittance of the perlite sample measured by the use of FTIR spectrometry and δ is the thickness of the pellet which is calculated by Eq. (11)

$$\delta = \frac{WP}{\rho^* A_{\text{KBr}}} \tag{11}$$

where W is the total mass of the sample pellet that contains both perlite and KBr, P is the mass percentage of perlite in the sample, ρ^* is the density of the core material in the FTIR pellet and A_{KBr} is the cross-

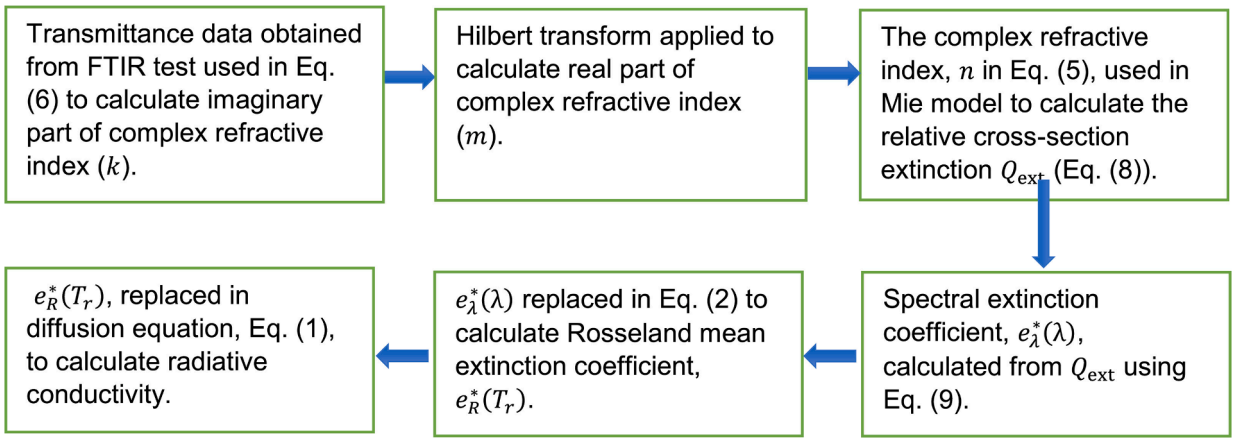

Flowchart 1. Steps of calculation of radiative conductivity using Mie model. (For interpretation of the references to color in this figure legend, the reader is referred to the web version of this article.)

sectional area of the pellet.

3. Mie model predictions

Fig. 1 shows a comparison between Mie model predictions and analytical solution for spectral mass-specific extinction coefficient, mass-specific Rosseland mean extinction coefficient and radiative conductivity. In Mie model simulations, different particle diameters (20, 30, 50, 100 μm) are selected for the perlite particles, and perlite density fixed at 230 kgm^{-3}. Based on Fig. 1a, increasing particle diameter decreases the peak value of spectral mass-specific extinction coefficient at 9.6 μm significantly. However, the peak reduction of spectral mass-specific extinction coefficient does not have major impact on Rosseland mean extinction coefficient and radiative conductivity. All particle diameters (20, 30, 50, 100 μm) produce similar value for the radiative conductivity. Fig. 1b and Fig. 1c, respectively, show that Rosseland mean extinction coefficient decreases at higher temperatures with minima at 650 K, whereas, radiative conductivity continuously increases as temperature rises. Overall, there is good agreement between Mie model predictions and the analytical solution. The discrepancies between the Mie model prediction and the analytical solution of the extinction coefficients and radiative conductivity are due to the fact that Beer's law, Eq. (10), is applied to the transmission measurement without considering the scattering in the original beam. Also, Mie model considers the effect of particle size when it calculates spectral mass-specific extinction coefficient. Beer's law, Eq. (10), does not consider the effect of particle size.

Fig. 2a reveals that the spectral mass-specific extinction coefficient for perlite with different densities (ρ = 230, 250 and 280 kgm^{-3}) have almost same value for the peak value (340–375 m^{2}kg^{-1}) at 9.6 μm. Fig. 2b and Fig. 2c, respectively, show that Rosseland mean extinction coefficient increases significantly with increasing density, however, radiative conductivity decreases significantly with increasing density.

4. Numerical model for solid and gaseous conductivity

Solid and gaseous heat transfer in perlite VIPs, respectively, occurs through solid matrix and gas molecules inside micro-pores. The validated numerical model developed by Verma and Singh [5] is used in the present study to calculate solid and gaseous conductivity. The simple cubic packing, in which each particle contacts with six neighbouring particles, is selected for geometrical design of perlite particles. Solid and gaseous conductivity in simple cubic packing can be calculated analytically [40], however, this analytical solution does not consider the three-dimensional heat flow within the particle. Therefore, the above-mentioned analytical solution is inaccurate. In the present study, the solid and gaseous conductivity are predicted numerically using finite element method.

Here, COMSOL Multiphysics 6.0 is the numerical solver for steady state heat transfer equation and the three-dimensional Fourier's law. A parametric geometry of the unit cells is developed and the solution domain is discretised using tetrahedral mesh.

The mesh size is characterised by minimum element size of 2.5 μm and maximum element size of 20 μm. The unit cells are subjected to a temperature difference of 20 °C between isothermally held upper and lower faces [5]. In the numerical model, the steady state heat transfer equation, Eq. (12), and the three-dimensional Fourier's law, Eq. (13), are the governing equations:

$$\frac{\partial}{\partial x}\left(\kappa_i\frac{\partial T}{\partial x}\right)+\frac{\partial}{\partial y}\left(\kappa_i\frac{\partial T}{\partial y}\right)+\frac{\partial}{\partial z}\left(\kappa_i\frac{\partial T}{\partial z}\right)=0 \tag{12}$$

$$\dot{Q}_{c,w}=-\kappa_i A\frac{\partial T}{\partial w} \tag{13}$$

where κ_i is either the thermal conductivity of the grain (κ_{gr}) or the gas inside pore (κ_g), T is the temperature, $\dot{Q}_{c,w}$ is the rate of heat conduction at a point on an isothermal surface that its normal is given by the vector w and A is the area of surface normal to the direction of heat flux. The total heat flux is used to obtain the thermal conductivity of the unit cell (κ_c) using Fourier's law on the whole unit cell:

$$\kappa_c=-\dot{Q}_u\frac{l_u}{A_u\,\Delta T_u} \tag{14}$$

where $\dot{Q}_u$ is the heat flux calculated at one of the faces of the unit cells, l_u is the length of the unit cell, A_u is the area of top/bottom surface of the unit cell and ΔT_u is the temperature difference between the two surfaces. Gaseous conductivity is a function of the pore size which is measurable from scanning electron microscope (SEM) images. In the present model, the gaseous conductivity is calculated through Kaganer model [41]:

$$\kappa_g=\frac{\kappa_g^0}{1+2\beta\frac{l_g}{D_p}} \tag{15}$$

$$l_g=\frac{\sigma T}{\sqrt{2}\pi d_g^2 p} \tag{16}$$

where κ_g is the gaseous conductivity of the pore, κ_g^0 the conductivity of free air, β the coefficient which depends on the accommodation coefficient and the adiabatic coefficient of the gas, l_g the mean free path length of gas inside the pore, D_p the characteristic dimension of the pore, σ the Boltzmann constant, d_g the molecular size of the gas and p is the internal

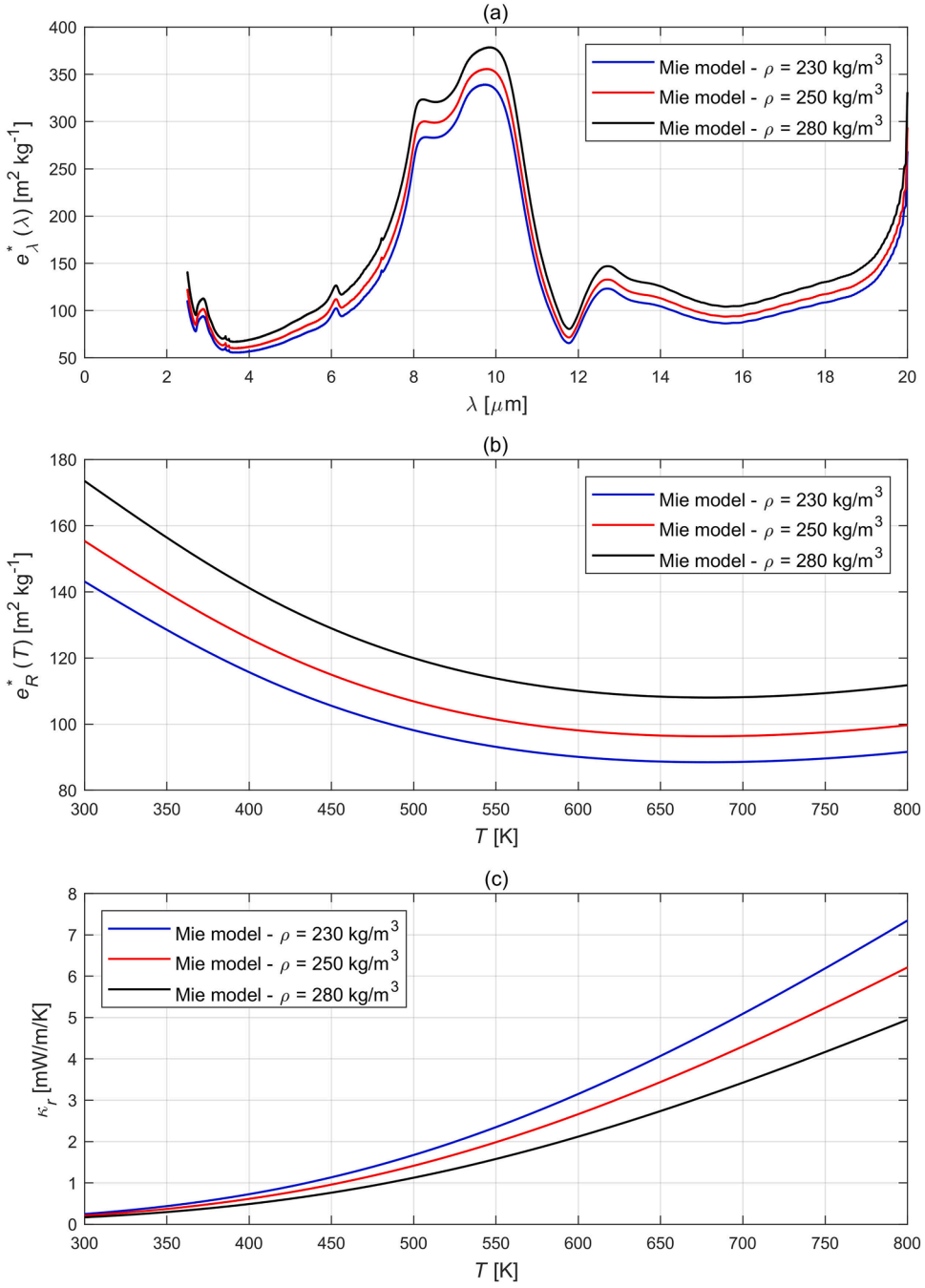

Fig. 2. Mie model predictions for perlite (D=30 μm) with different densities ρ = 230, 250 and 280 kgm^{-3}. (*a*) spectral mass-specific extinction coefficient (*b*) mass-specific Rosseland mean extinction coefficient and (*c*) radiative conductivity. (For interpretation of the references to color in this figure legend, the reader is referred to the web version of this article.)

gas pressure.

In the present model, grain's or particle's thermal conductivity (κ_{gr}) is an input parameter which is calculated using Russel's equation:

$$\kappa_{gr} = \kappa_T \times \left(\frac{\xi^{2/3} + \nu\left(1 - \xi^{2/3}\right)}{\xi^{2/3} - \xi + \nu\left(1 - \xi^{2/3} + \xi\right)} \right) \tag{17}$$

where κ_T is the thermal conductivity of the bulk material (SiO_2 for perlite), ξ is the grain porosity, ν is the ratio of κ_T and κ_g (Eq. (15)). Porosity of the perlite grain, ξ, is obtained using Eq. (18):

$$\xi = \frac{(\gamma - 1) + \phi_i}{\gamma} \tag{18}$$

where γ is the multiplication factor of increase in the particle's volume after rapid heating and ϕ_i the perlite grain initial porosity. For more details about the developed finite element numerical model see Verma and Singh [5].

Fig. 3 shows (*a*) geometry of simple cubic packing, (*b*) mesh distribution, (*c*) temperature distribution and (*d*) mesh independence test for the numerical model developed. Four different numbers of mesh elements, mesh categories, were selected to perform mesh independence test. These categories are coarser, coarse, normal and fine. The number of elements are 15,933, 32,328, 75,952 and 832,150 for coarser, coarse, normal and fine mesh categories, respectively. It is obvious in Fig. 3d that normal mesh category provides accurate prediction for solid and

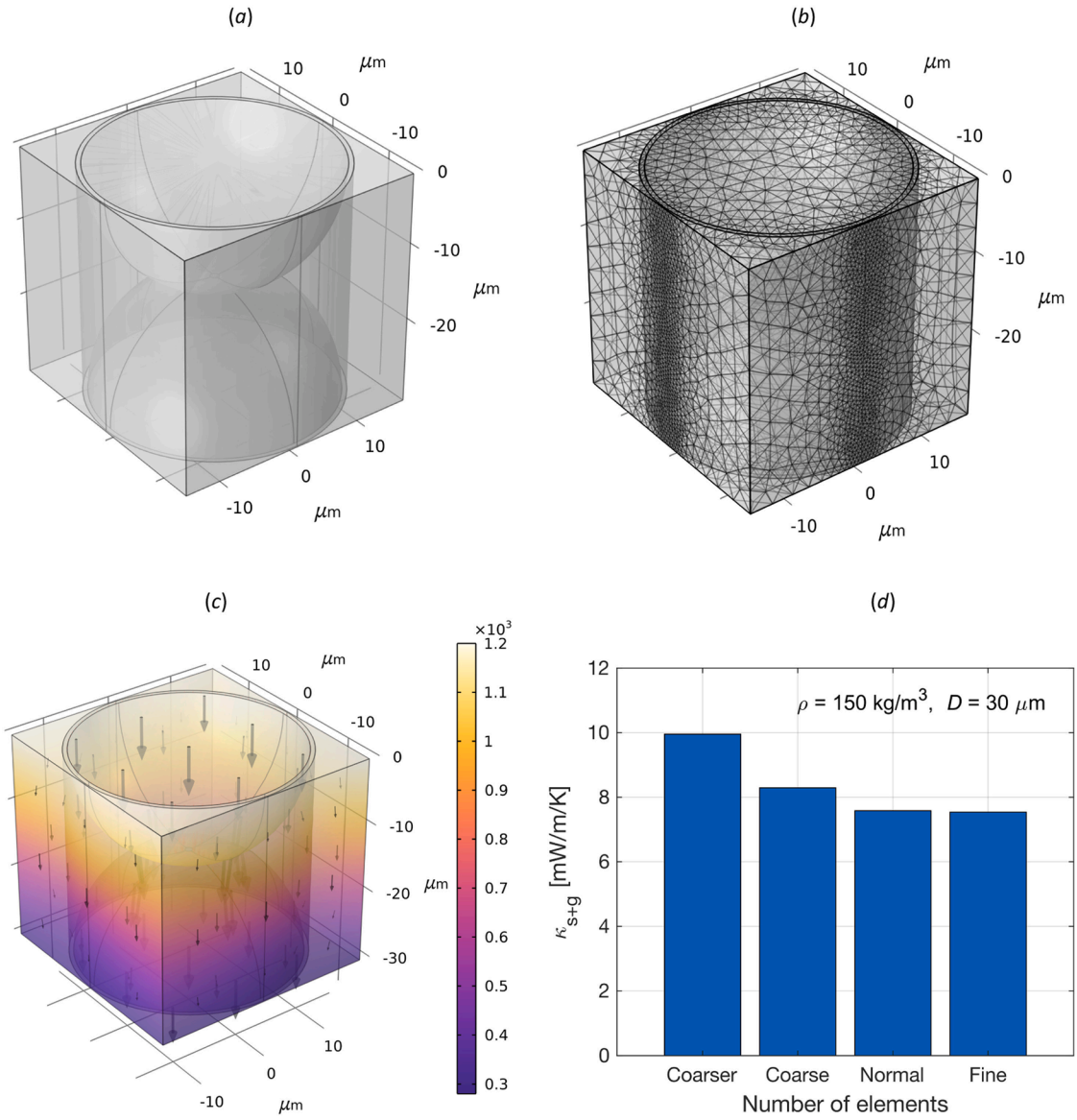

Fig. 3. The output of numerical model for the (*a*) geometry of simple cubic packing, (*b*) mesh distribution, (*c*) temperature distribution and (*d*) mesh independence test. (For interpretation of the references to color in this figure legend, the reader is referred to the web version of this article.)

gaseous thermal conductivities, 7.57 mW/m/K, and fine mesh category does not increase the accuracy of prediction. Therefore, normal mesh category is selected to perform all numerical predictions. It is worth mentioning that perlite sample with density of 150 kgm^{-3} and particle diameter of 30 μm at temperature of 300 K was selected for the mesh independence test.

5. Numerical predictions of the coupled model for the solid, gaseous and radiative conductivities

This section presents the numerical predictions of the developed finite element model and Mie model. The value of solid, gaseous and radiative thermal conductivity is calculated for the perlite VIPs. Fig. 4 shows total thermal conductivity at different temperatures for internal gas pressure of 0.1 mbar. Increasing the density increases the solid and gaseous conductivities at (*a*) 300 K, (*b*) 400 K, (*c*) 500 K, (*d*) 600 K, (*e*) 700 K and (*f*) 800 K. However, increasing the density decreases radiative conductivity. Here the perlite particle diameter is $D = 30$ μm. The contribution of radiative thermal conductivity to total thermal conductivity increases as the temperature is increased. Radiative conductivity is significantly more at higher temperatures ((*d*) 600 K, (*e*) 700 K and (*f*) 800 K).

At 700 K the smallest density of 150 kgm^{-3} and the largest density of 280 kgm^{-3} produce the highest total thermal conductivity (≈ 21 mW/m/K). The smallest density causes the highest radiative conductivity, whereas, the largest density produces the highest solid and gaseous conductivity. An inverted bell curve is traced by total thermal conductivity as density varies at higher temperatures ≥ 600 K with minima shifting towards a higher density (see Fig 4 (d-f)). For example, at 600 K, density of 180 kgm^{-3} produces the lowest total thermal conductivity of ≈ 16 mW/m/K and, at 700 K, density of 210 kgm^{-3} produces the lowest total thermal conductivity of 19 mW/m/K (see Fig. 4d and e).

Fig. 5 shows contribution of each heat transfer mechanism to total thermal conductivity. Fig 5a presents contribution of radiative conductivity to total thermal conductivity and Fig. 5b depicts contribution of solid and gaseous conductivities to total thermal conductivity at 300, 400, 500, 600, 700 and 800 K, respectively.

For instance, total thermal conductivity of perlite with density of 150 kgm^{-3} at 800 K includes 65 % contribution of radiative conductivity and 35 % contribution of solid and gaseous conductivities (see black

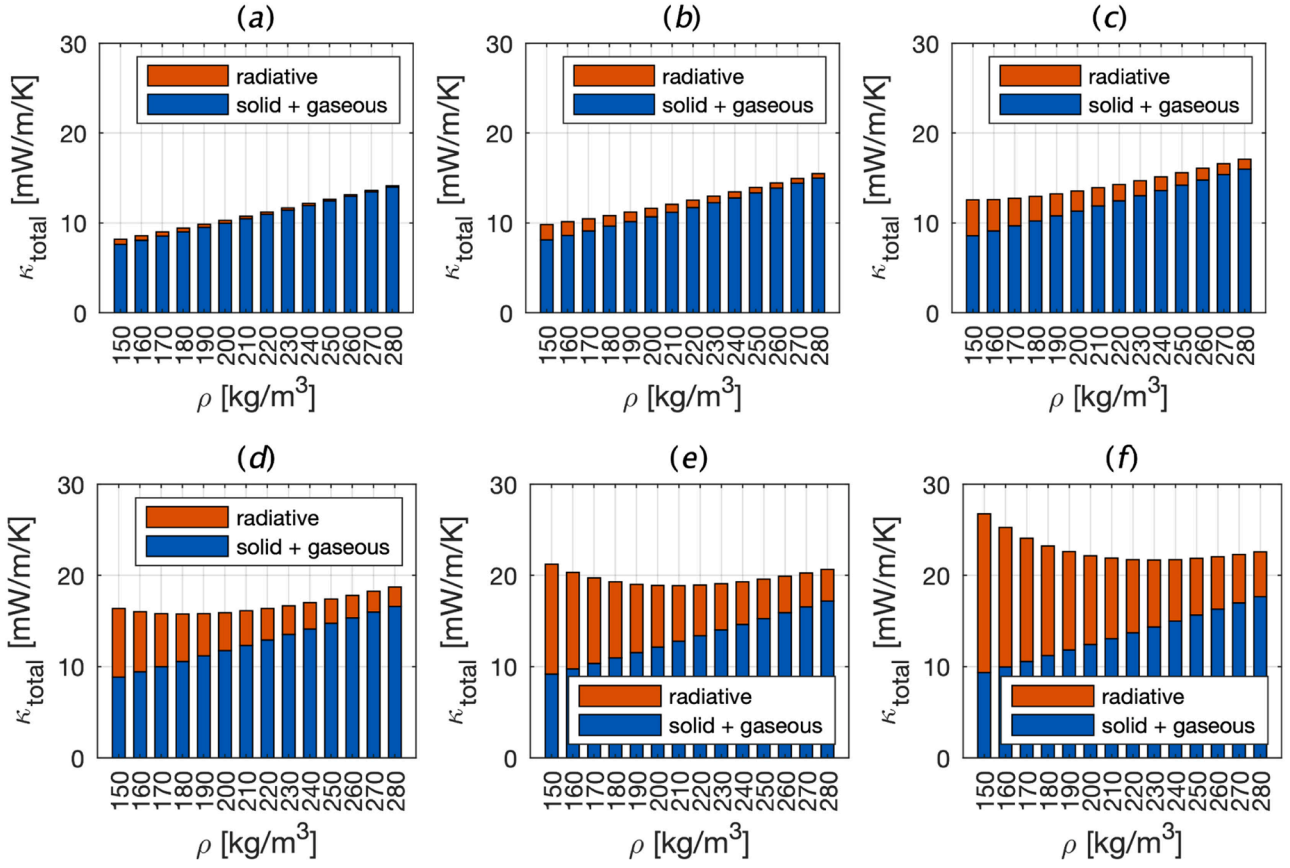

Fig. 4. The coupled model predictions of solid, gaseous and radiative conductivities at (*a*) 300 K, (*b*) 400 K, (*c*) 500 K, (*d*) 600 K, (*e*) 700 K and (*f*) 800 K for VIPs sealed at 0.1 mbar. (For interpretation of the references to color in this figure legend, the reader is referred to the web version of this article.)

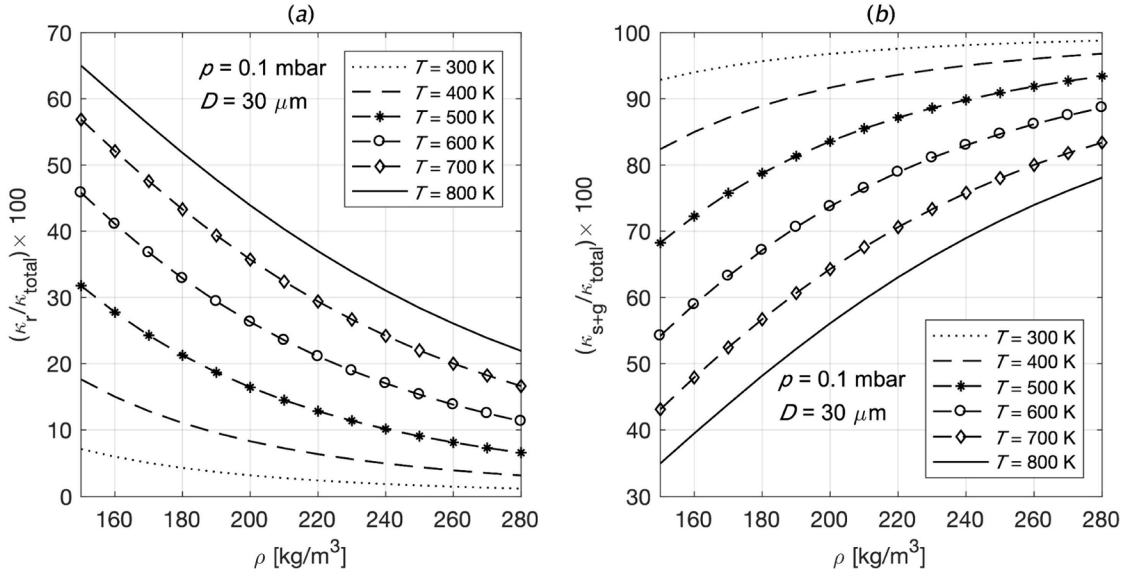

Fig. 5. Contribution of each heat transfer mechanism to total thermal conductivity at 300, 400, 500, 600, 700 and 800 K: (*a*) contribution of radiative conductivity to total thermal conductivity (*b*) contribution of solid and gaseous conductivities to total thermal conductivity.

solid line Fig. 5a and b). At 300 K, total thermal conductivity of perlite with density of 150 kgm^{-3} includes 8 % contribution of radiative conductivity and 92 % contribution of solid and gaseous conductivities (see dotted line Fig. 5a and b). In another example, total thermal conductivity of perlite with density of 280 kgm^{-3} at 800 K includes 21 % contribution of radiative conductivity and 79 % contribution of solid and gaseous conductivities (see black solid line Fig. 5a and b). At 300 K, total thermal conductivity of perlite with density of 280 kgm^{-3} includes 1 % contribution of radiative conductivity and 99 % contribution of solid and gaseous conductivities (see dotted line Fig 5a and b).

Fig. 6 presents the importance of radiative conductivity at high temperatures where three densities ((*a*) 150 kgm^{-3}, (*b*) 230 kgm^{-3}, (*c*)

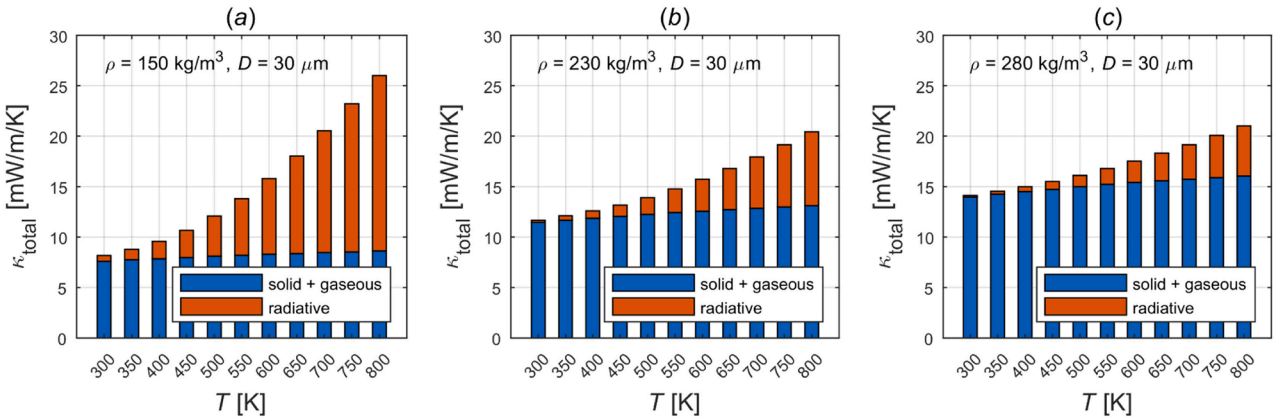

Fig. 6. The contribution of radiative conductivity to the total thermal conductivity for three densities (*a*) 150 kgm^{-3}, (*b*) 230 kgm^{-3}, (*c*) 280 kgm^{-3}. (For interpretation of the references to color in this figure legend, the reader is referred to the web version of this article.)

280 kgm^{-3}) are used. As it is clear from Fig. 6a, at temperatures above 600 K radiative conductivity of perlite with the smallest density (150 kg m^{-3}) is larger than the solid and gaseous conductivities altogether. This phenomenon does not occur at higher densities studied (Fig. 6b and c). Increasing the density to 280 kgm^{-3} significantly reduces radiative conductivity to 5 mW/m/K with almost negligible effect on solid and gaseous conductivities (16 mW/m/K) at 800 K, see Fig. 6(c).

Fig. 7 shows the effect of density and particle diameter on radiative thermal conductivity at different temperatures. Fig. 7a reveals that radiative conductivity rapidly decreases with increasing density at higher temperatures $T \geq 500$ K. For instance, at 800 K, radiative conductivity decreases from 17.4 mW/m/K to 5 mW/m/K when density increases from 150 kgm^{-3} to 280 kgm^{-3}. As it is shown in Fig. 7a, at lower temperatures (300, 400 and 500 K) increase in density results into a gradual reduce in the radiative conductivity, however, at higher temperatures (600, 700 and 800 K) reduce is comparatively steeper. Note, particle diameter is 30 μm in Fig. 7a. It is evident from Fig. 7b that increasing the particle diameter does not have major impact on radiative conductivity at higher temperatures (600, 700 and 800 K). Fig. 7b shows that increasing the temperature results into rise in the radiative conductivity. For all particle sizes, at lower temperatures (300 and 400 K) radiative conductivity is low (∼0.24 mW/m/K), whereas it has a high value (∼7 mW/m/K) at higher temperatures (700 and 800 K). Note, density of sample is 230 kgm^{-3} in Fig. 7b.

Fig. 8 shows the total thermal conductivity predicted by the coupled model for different densities (150, 230, 280 kgm^{-3}) with fixed particle diameter of 30 μm. At the lowest temperature (300 K), the smallest density 150 kgm^{-3} produces the smallest value of total thermal conductivity (8 mW/m/K). However, at the highest temperature (1200 K), the largest density 280 kgm^{-3} produces the smallest value for total thermal conductivity of 28 mW/m/K. At highest temperature, sample with density of 150 kgm^{-3} produces the highest value of total conductivity (48 mW/m/K), most of which is contributed by radiative conductivity component (see Fig. 7a). Sample with density of 230 kgm^{-3} produces total thermal conductivity of 31 mW/m/K at the highest temperature (1200 K).

Fig. 8 reveals interesting observations, for instance:

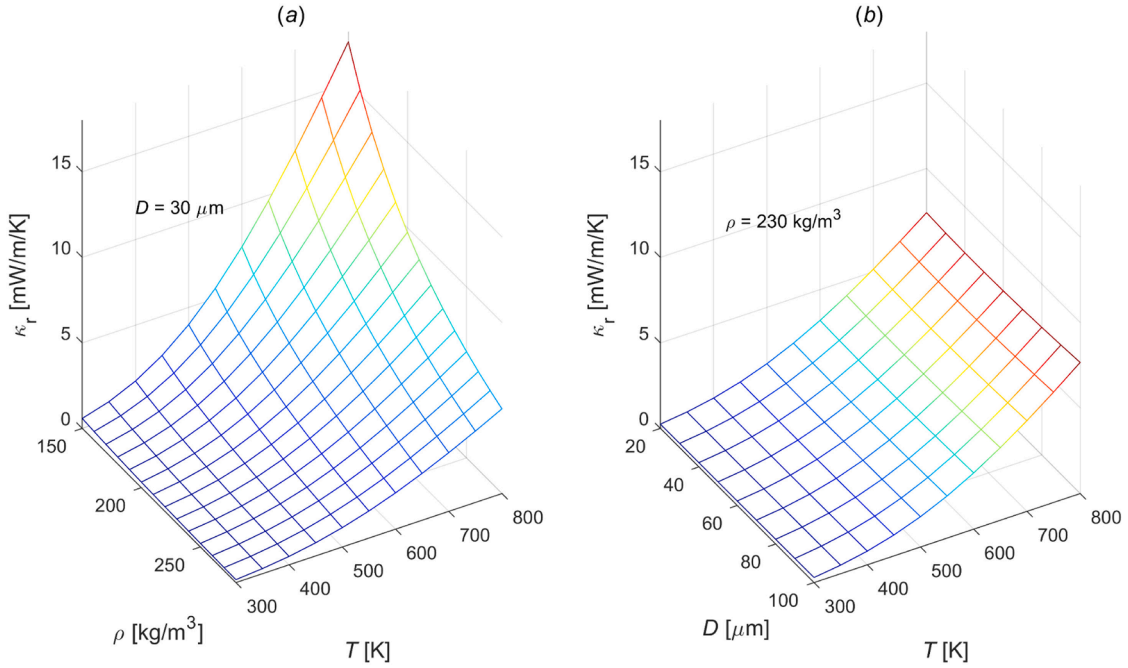

Fig. 7. The effect of density (*a*) and particle diameter (*b*) on radiative conductivity. (For interpretation of the references to color in this figure legend, the reader is referred to the web version of this article.)

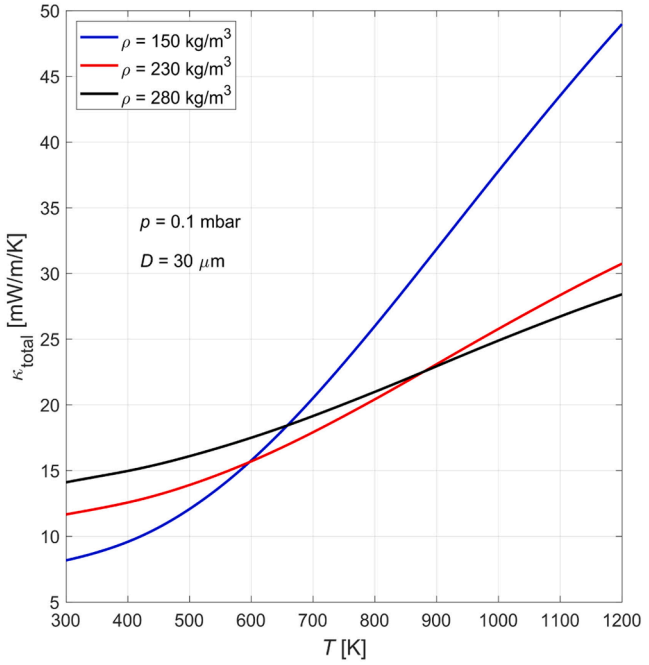

Fig. 8. The effect of density on total thermal conductivity. (For interpretation of the references to color in this figure legend, the reader is referred to the web version of this article.)

(i) at 597 K, the densities of 150 and 230 kgm^{-3} produce the same value for the total thermal conductivity (15.7 mW/m/K).
(ii) at 658 K, the densities of 150 and 280 kgm^{-3} produce the same value for the total thermal conductivity (18.5 mW/m/K). and
(iii) at 879 K, the densities of 230 and 280 kgm^{-3} produce the same value for the total thermal conductivity (22.5 mW/m/K).

This means that although the contribution of radiative conductivity is high for the sample with density of 150 kgm^{-3}, the contribution of solid and gaseous conductivity is low. In contrast, for the sample with density of 280 kgm^{-3} the contribution of radiative conductivity is low but the contribution of solid and gaseous conductivity is high. Therefore, at a specific temperature, different densities can produce the same value for the total thermal conductivity giving the VIP developers and manufacturers a choice to pick the density that best suits their design criteria, such as cost effectiveness.

6. Experimental validation of coupled model predictions of the solid, gaseous and radiative conductivities

The total thermal conductivity is measured experimentally by means of the transient hot-wire technique to validate the coupled model predictions at different temperatures (300, 491, 557 and 767 K). In the hot-wire method, a platinum wire is embedded in the perlite sample sealed at 0.1 mbar. The density of perlite is 150 kgm^{-3}. The wire acts as heating element and temperature sensor simultaneously. The wire is heated with a constant electrical power during the experiment. The development of the hot-wire temperature over time is obtained using the temperature dependant resistance of the wire. Hot-wire temperature evaluations depend on the thermal conductivity of the sample. Fitting an analytical solution [42] to the temperature over time curve yields the thermal conductivity of the perlite sample. Several measurement curves are averaged to minimise the statistical uncertainty.

Fig. 9a shows comparison between numerical predictions and experimental measurements of total thermal conductivity at 300, 491, 557 and 767 K. As it is seen in Fig. 9a, there is excellent agreement between numerical predictions of coupled model and experimental measurements at 300, 491, 557 and 767 K. The value of total thermal conductivity for numerical predictions and experimental measurements at 300, 491, 557 and 767 K are shown in Table 1.

Table 1
Comparison between numerical predictions and experimental measurements of total thermal conductivity.

T	κ_{total} (numerical)	κ_{total} (experimental)
300 K	8.2 mW/m/K	9±0.5 mW/m/K
491 K	12.3 mW/m/K	13.2±0.9 mW/m/K
557 K	14.6 mW/m/K	14.7±1.2 mW/m/K
767 K	25 mW/m/K	20.5±1.8 mW/m/K

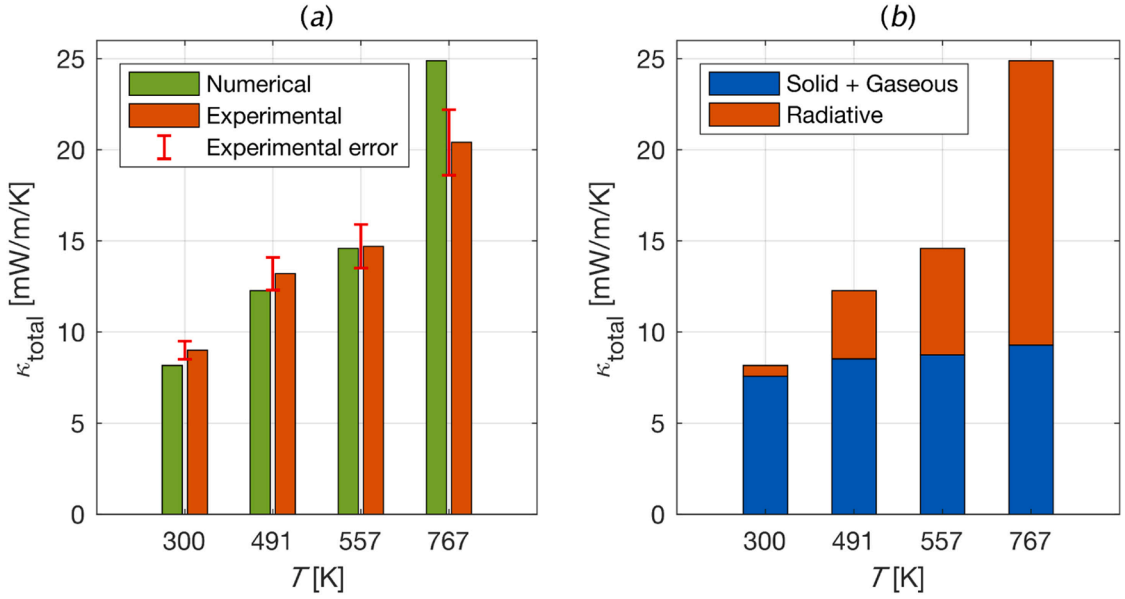

Fig. 9. (*a*): Comparison between numerical predictions and experimental measurements of total thermal conductivity at $T = 300$, 491, 557 and 767 K. Density of VIP is 150 kgm^{-3} and it is sealed at 0.1 mbar. (*b*): numerical predictions of contribution of solid, gaseous and radiative conductivities to total thermal conductivity at $T =$ 300, 491, 557 and 767 K. (For interpretation of the references to color in this figure legend, the reader is referred to the web version of this article.)

At 767 K, small deviation between numerical prediction and experimental measurement of total thermal conductivity is observable. The numerical prediction of total thermal conductivity, κ_{total} (numerical), at 767 K is 25 mW/m/K and the experimental measurement of total thermal conductivity, κ_{total} (experimental), is 22.5 mW/m/K. This difference is due to an experimental error which occurs in the measurement of perlite density. It is very difficult to prepare a perlite sample with exact density of 150 kgm^{-3} and we considered $\pm$5 kgm^{-3} as an error in density measurement. This error has direct impact on experimentally measured total conductivity (most of which influences radiative conductivity) at 767 K. Moreover, an error of $\pm$3 K is associated with the highest temperature (767 K$\pm$3 K) of experimental measurement.

The coupled model predictions of the contribution of each heat transfer mechanism (solid, gaseous and radiative conductivities) to total thermal conductivity at 300, 491, 557 and 767 K are shown in Table 2. Here, κ_{s+g} is solid and gaseous thermal conductivities and κ_r is radiative conductivity. Also, the contribution of solid, gaseous and radiative conductivities to total thermal conductivity are shown in Fig 9b. It becomes clear that the radiative conductivity contributes more to total thermal conductivity at higher temperatures 491, 557 and 767 K. The contribution of radiative conductivity to total thermal conductivity is negligible at room temperature $T = 300$ K. In summary, experimental validation of coupled model predictions shows the capability of the developed model in predictions of total thermal conductivity at high temperatures.

7. Conclusion

In the present study, we developed a coupled numerical model which has the capability to predict total thermal conductivity over range of 300–800 K. The present study is novel and original, because it is the first model that combines the finite element based solid and gaseous conductivity model with Mie theory. The developed model accurately predicts total thermal conductivity at high temperatures $\geq$500 K. High temperature application is the main advantage of the present model over previously developed numerical models. The newly developed coupled model is successfully validated against experimental measurements at high temperatures. The coupled model includes the numerical model developed by Verma and Singh [5] and Mie model. Developed model by [5] approximates solid and gaseous conductivities and Mie model estimates radiative conductivity. Total thermal conductivity is simply calculated by adding solid and gaseous conductivities to radiative conductivity. The output of Mie model is verified against analytical solution, Beer's law, and there exists good agreement between them. The discrepancy between the Mie model prediction and the analytical solution is due to the fact that analytical solution neglects the effect of particle size when it calculates spectral mass-specific extinction coefficient. Several numerical tests have been performed to show the effect of perlite density and particle size on radiative and total thermal conductivities. The main findings are:

- All particle diameters of perlite (20μm– 100μm) produce similar values of radiative conductivity. Therefore, density is found be the main property of perlite responsible for reducing radiative conductivity (see Fig. 1 and 2).
- Mie model predicted that Rosseland mean extinction coefficient increases significantly with increasing density and concomitantly radiative conductivity decreases significantly with an increasing density (see Fig. 2).
- Radiative conductivity of perlite rapidly decreases with increasing density at higher temperatures $\geq$ 500 K. For instance, at 800 K, radiative conductivity decreased from 17.4 mW/m/K to 5 mW/m/K when density increased from 150 kgm^{-3} to 280 kgm^{-3} (see Fig. 7a).
- At lower temperatures (300–400 K), the smallest density of perlite (150 kgm^{-3}) results into the lowest value of total thermal conductivity of 8 mW/m/K for VIPs sealed at 0.1 mbar (see Fig. 4a and b).

Table 2
Coupled model predictions of the contribution of each heat transfer mechanism (solid, gaseous and radiative conductivities) to total thermal conductivity.

T	κ_{s+g}	κ_r
300 K	7.6 mW/m/K	0.6 mW/m/K
491 K	8.5 mW/m/K	3.8 mW/m/K
557 K	8.7 mW/m/K	5.9 mW/m/K
767 K	9.4 mW/m/K	15.6 mW/m/K

- At higher temperatures (500–800 K) smaller density does not produce a lower total thermal conductivity. For instance, at 700 K a mid-level density, 210 kgm^{-3}, produces the lowest total thermal conductivity. In the present study, densities from 150 to 280 kgm^{-3} were studied with an increment of 10 kgm^{-3}, (see Fig 4c).
- A nonlinear curve is traced by total thermal conductivity as density varied at higher temperatures $\geq$ 600 K with minima shifting towards a higher density (see Fig. 4 (d-f)).
- There is excellent agreement between numerical predictions of coupled model and experimental measurements of total thermal conductivity at 300, 491, 557 and 767 K (see Fig. 9a).

Declaration of generative AI in scientific writing

AI was not used for writing process of the manuscript.

CRediT authorship contribution statement

Mohammad Reza Jalali: Conceptualization, Methodology, Formal analysis, Data curation, Software, Writing – original draft. **Dron Kaushik:** Conceptualization, Methodology, Formal analysis, Software, Visualization. **Sankarshan Verma:** Conceptualization, Methodology, Software, Formal analysis. **Harjit Singh:** Conceptualization, Methodology, Project administration, Supervision, Resources, Writing – review & editing.

Declaration of Competing Interest

The authors declare that they have no known competing financial interests or personal relationships that could have appeared to influence the work reported in this paper.

Data availability

Data will be made available on request.

References

[1] M. Khudaykulova, H. Yuanqiong, A. Khudaykulov, Economic consequences and implications of the Ukraine-Russia War, Int. J. Manag. Sci. Bus. Admin. 8 (2022) 44–52, https://doi.org/10.18775/ijmsba.1849-5664-5419.2014.84.1005.
[2] M. Alam, H. Singh, S. Brunner, C. Naziris, Experimental characterisation and evaluation of the thermo-physical properties of expanded perlite—Fumed silica composite for effective vacuum insulation panel (VIP) core, Energy Build. 69 (2014) 442–450, https://doi.org/10.1016/j.enbuild.2013.11.027.
[3] H. Singh, M. Geisler, F. Menzel, Experimental investigations into thermal transport phenomena in vacuum insulation panels (VIPs) using fumed silica cores, Energy Build. 107 (2015) 76–83, https://doi.org/10.1016/j.enbuild.2015.08.004.
[4] M. Rottmann, T. Beikircher, H.P. Ebert, Thermal conductivity of evacuated expanded perlite measured with guarded-hot-plate and transient-hot-wire method at temperatures between 295 K and 1073 K, Int. J. Therm. Sci. 152 (2020), 106338, https://doi.org/10.1016/J.IJTHERMALSCI.2020.106338.
[5] S. Verma, H. Singh, Predicting the conductive heat transfer through evacuated perlite based vacuum insulation panels, Int. J. Therm. Sci. 171 (2022), 107245, https://doi.org/10.1016/j.ijthermalsci.2021.107245.
[6] S. Verma, A. Sara, H. Singh, Why and which opacifier for perlite based vacuum insulation panels (VIPs) in the average temperature range of 10–70 °C, Int. J. Therm. Sci. 186 (2023), 108136, https://doi.org/10.1016/j.ijthermalsci.2022.108136.

[7] T. Beikircher, M. Demharter, Heat transport in evacuated perlite powders for super-insulated long-term storages up to 300 °C, J. Heat Transf. 135 (2013), https://doi.org/10.1115/1.4023351.
[8] M. Rottmann, T. Beikircher, H.P. Ebert, F. Hemberger, J. Manara, Thermal conductivity and extinction coefficient of opacified expanded perlite for vacuum super insulation up to 1073 K, Int. J. Therm. Sci. 163 (2021), https://doi.org/10.1016/j.ijthermalsci.2020.106813.
[9] Y. Liang, H. Wu, G. Huang, J. Yang, Y. Ding, Prediction and optimization of thermal conductivity of vacuum insulation panels with aerogel composite cores, Proc. Eng. 205 (2017) 2855–2862, https://doi.org/10.1016/J.PROENG.2017.09.909.
[10] D. Baillis, J.F. Sacadura, Thermal radiation properties of dispersed media: theoretical prediction and experimental characterization, J. Quant. Spectrosc. Radiat. Transf. 67 (2000) 327–363, https://doi.org/10.1016/S0022-4073(99)00234-4.
[11] A. Kan, L. Kang, C. Wang, D. Cao, A simple and effective model for prediction of effective thermal conductivity of vacuum insulation panels, Fut. Cities Environ. 1 (2015) 4, https://doi.org/10.1186/S40984-015-0001-Z.
[12] C. Jang, J. Kim, T.H. Song, Combined heat transfer of radiation and conduction in stacked radiation shields for vacuum insulation panels, Energy Build. 43 (2011) 3343–3352, https://doi.org/10.1016/J.ENBUILD.2011.08.036.
[13] G. Foray, J.H. Randrianalisoa, J. Adrien, E. Maire, X-ray tomography coupled with finite elements, a fast method to design aerogel composites and prove their superinsulation experimentally, Gels 8 (2022) 732, https://doi.org/10.3390/gels8110732.
[14] M. Bouquerel, T. Duforestel, D. Baillis, G. Rusaouen, Heat transfer modeling in vacuum insulation panels containing nanoporous silicas - A review, Energy Build. 54 (2012) 320–336, https://doi.org/10.1016/J.ENBUILD.2012.07.034.
[15] B.M. Zhang, S.Y. Zhao, X.D. He, Experimental and theoretical studies on high-temperature thermal properties of fibrous insulation, J. Quant. Spectrosc. Radiat. Transf. 109 (2008) 1309–1324, https://doi.org/10.1016/J.JQSRT.2007.10.008.
[16] J. Yang, H. Wu, S. He, M. Wang, Prediction of thermal conductivity of fiber/aerogel composites for optimal thermal insulation, J. Porous Media 18 (2015) 971–984, https://doi.org/10.1615/JPORMEDIA.2015013550.
[17] R. Caps, A. Trunzer, D. Büttner, J. Fricke, H. Reiss, Spectral transmission and reflection properties of high temperature insulation materials, Int. J. Heat Mass Transf. 27 (1984) 1865–1872, https://doi.org/10.1016/0017-9310(84)90168-6.
[18] J. Yang, H. Wu, M. Wang, S. He, H. Huang, Prediction and optimization of radiative thermal properties of ultrafine fibrous insulations, Appl. Therm. Eng. 104 (2016) 394–402, https://doi.org/10.1016/j.applthermaleng.2016.05.062.
[19] C. Jang, H. Jung, J. Lee, T.H. Song, Radiative heat transfer analysis in pure scattering layers to be used in vacuum insulation panels, Appl. Energy 112 (2013) 703–709, https://doi.org/10.1016/J.APENERGY.2013.04.038.
[20] B. Choi, J. Lee, T.H. Song, Investigation of radiative scattering effect of VIP filler materials using a novel statistical formulation, Int. J. Heat Mass Transf. 89 (2015) 339–344, https://doi.org/10.1016/J.IJHEATMASSTRANSFER.2015.05.047.
[21] T. Xie, Y.L. He, Z.J. Hu, Theoretical study on thermal conductivities of silica aerogel composite insulating material, Int. J. Heat Mass Transf. 58 (2013) 540–552, https://doi.org/10.1016/j.ijheatmasstransfer.2012.11.016.
[22] H. Liu, X. Xia, Q. Ai, X. Xie, C. Sun, Experimental investigations on temperature-dependent effective thermal conductivity of nanoporous silica aerogel composite, Exp. Therm. Fluid Sci. 84 (2017) 67–77, https://doi.org/10.1016/J.EXPTHERMFLUSCI.2017.01.021.
[23] M. Arduini, J. Manara, C. Vo, Modeling of radiative properties of polystyrene foams containing IR-opacifiers, Cell. Poly. 35 (2016).
[24] J. Feng, D. Chen, W. Ni, S. Yang, Z. Hu, Study of IR absorption properties of fumed silica-opacifier composites, J. Non Cryst. Solids 356 (2010) 480–483, https://doi.org/10.1016/J.JNONCRYSOL.2009.12.015.
[25] C.Y. Zhu, Z.Y. Li, H.Q. Pang, N. Pan, Design and optimization of core/shell structures as highly efficient opacifiers for silica aerogels as high-temperature thermal insulation, Int. J. Therm. Sci. 133 (2018) 206–215, https://doi.org/10.1016/J.IJTHERMALSCI.2018.07.032.
[26] K.Y. Wang, C.L. Tien, Radiative heat transfer through opacified fibers and powders, J. Quant. Spectrosc. Radiat. Transf. 30 (1983) 213–223, https://doi.org/10.1016/0022-4073(83)90059-6.
[27] R. Caps, J. Fricke, Thermal conductivity of opacified powder filler materials for vacuum insulations1, Int. J. Thermophys. 21 (2) (2000) 445–452, https://doi.org/10.1023/A:1006691731253.
[28] J. Feng, Y. Wang, X. Feng, Q. Huang, S. Ma, W. Mo, J. Yang, X. Su, M. Lin, Radiative heat attenuation mechanisms for nanoporous thermal insulating composites, Appl. Therm. Eng. 105 (2016) 39–45, https://doi.org/10.1016/j.applthermaleng.2016.05.136.
[29] J. Kuhn, S. Korder, M.C. Arduini-Schuster, R. Caps, J. Fricke, Infrared-optical transmission and reflection measurements on loose powders, Rev. Sci. Instrum. 64 (1998) 2523, https://doi.org/10.1063/1.1143914.
[30] N.E. Hager, R.C. Steere, Radiant heat transfer in fibrous thermal insulation, J. Appl. Phys. 38 (1967) 4663, https://doi.org/10.1063/1.1709200.
[31] Baillis D., Raynaud M., Sacadura J.F., Determination of Spectral Radiative Properties of Open Cell Foam: model Validation, 14 (2012) 137–143. doi:10.2514/2.6519.
[32] T.W. Tong, C.L. Tien, Radiative heat transfer in fibrous insulations—Part I: analytical study, J. Heat Transf. 105 (1983) 70–75, https://doi.org/10.1115/1.3245561.
[33] J. Fricke, R. Caps, Heat transfer in thermal insulations—Recent progress in analysis, Int. J. Thermophys. 9 (5) (1988) 885–895, https://doi.org/10.1007/BF00503253.
[34] S. Sonnick, M. Meier, J. Ross-Jones, L. Erlbeck, I. Medina, H. Nirschl, M. Rädle, Correlation of pore size distribution with thermal conductivity of precipitated silica and experimental determination of the coupling effect, Appl. Therm. Eng. 150 (2019) 1037–1045, https://doi.org/10.1016/J.APPLTHERMALENG.2019.01.074.
[35] S. Arridge, P. van der Zee, D.T. Delpy, M. Cope, Particle sizing in the Mie scattering region: singular-value analysis, Inverse Probl. 5 (1989) 671–689, https://doi.org/10.1088/0266-5611/5/5/002.
[36] K.A. Whittaker, J. Keaveney, I.G. Hughes, C.S. Adams, Hilbert transform: applications to atomic spectra, Phys. Rev. A (Coll. Park) 91 (2015), 032513, https://doi.org/10.1103/PhysRevA.91.032513.
[37] C.F. Bohren, D.R. Huffman, Absorption and Scattering of Light by Small Particles, Wiley, 1998, https://doi.org/10.1002/9783527618156.
[38] B.E. Reed, D.M. Peters, R. McPheat, A.J.A. Smith, R.G. Grainger, Mass extinction spectra and size distribution measurements of quartz and amorphous silica aerosol at 0.33–19 μm compared to modelled extinction using Mie, CDE, and T -matrix theories, J. Quant. Spectrosc. Radiat. Transf. 199 (2017) 52–65, https://doi.org/10.1016/j.jqsrt.2017.05.011.
[39] H. Reiss, Radiative Transfer in Nontransparent, Dispersed Media, 1st ed., Springer Tracts in Modern Physics, Berlin, 1988.
[40] S.Q. Zeng, A. Hunt, R. Greif, Geometric structure and thermal conductivity of porous medium silica aerogel, J. Heat Transf. 117 (1995) 1055–1058, https://doi.org/10.1115/1.2836281.
[41] M.G. Kaganer, Thermal insulation in cryogenic engineering, Israel program for scientific translations, 1969.
[42] H.-P. Ebert, V. Bock, O. Nilsson, J. Fricke, The hot-wire method applied to porous materials of low thermal conductivity, High Temp.-High Press. 25 (1993) 391–402.